Journal of Power Sources 196 (2011) 10191–10200

Contents lists available at SciVerse ScienceDirect

Journal of Power Sources

journal homepage: www.elsevier.com/locate/jpowsour

Direct synthesis and coating of advanced nanocomposite negative electrodes for Li-ion batteries via electrospraying

M. Valvo, E. García-Tamayo*, U. Lafont, E.M. Kelder

NanoStructured Materials, ChemE, Delft University of Technology, Julianalaan 136, 2628 BL Delft, The Netherlands

ARTICLE INFO

Article history:
Received 28 April 2011
Received in revised form 4 August 2011
Accepted 11 August 2011
Available online 22 August 2011

Keywords:
Electrospray pyrolysis
Li-ion batteries
Nanocomposite electrodes
Metal oxides
PVdF

ABSTRACT

A direct approach for the synthesis and coating of advanced nanocomposite negative electrodes via a single-step process at low temperature is presented. Metal-oxide/PVdF nanocomposites are obtained in one step by electrospray pyrolysis of precursor solutions containing dissolved metal salts together with polyvinylidene fluoride (PVdF) as binder. In this way, small oxide nanoparticles are generated and dispersed in situ in the binder creating nanocomposite structures, while being coated at once as thin electrode layers on stainless steel coin cell cans. The intimate contact between the nanoparticles and the binder favours enhanced adhesion of the materials in the overall electrode structure and adequate electrochemical performances are obtained without any conductive additive. Three nanocomposite oxide/PVdF materials (i.e. SnO_2, CoO and Fe_2O_3) are reported here as preliminary examples of negative electrodes. The results show that this approach is suitable, not only for the fabrication of nanocomposite electrodes for Li-ion batteries, but also for other novel applications.

1. Introduction

Rechargeable Li-ion batteries represent a well-established technology for energy storage, being nowadays the most popular power source in portable electronics. The increasing miniaturization of microelectronic devices continuously challenges the performances achievable by conventional Li-ion batteries based on bulk, micrometer-sized materials. Even more stringent are the requirements to be met by advanced Li-ion batteries for electric and hybrid-electric vehicles, in terms of energy and power densities. The development of alternative routes towards higher storage capacities relies on the use of metals and transition metal oxides that can reversibly incorporate more Li than intercalation materials. Li-alloying with metals or semiconductors in various systems [1–5], as well as conversion reactions in interstitial-free *3d* metal oxide structures [6,7], are viable mechanisms to achieve large reversible capacities in negative electrodes. In particular, these materials are able to deliver capacities much higher than that of graphite (i.e. 372 mAh g^{-1} for LiC_6). However, the mechanical stability of Li-alloys is negatively affected by remarkable volume variations (i.e. up to ≈300%) that occur during uptake and removal of Li [8–10]. Transition metal oxides suffer from intrinsic shortcomings of large separation of the voltage on charge and discharge [11] and of volume changes, even though they are not as severe as those of Li-alloys [12]. Indeed, incorporation of more Li invariably results in an increase of the volume of the host materials, which undergo major structural changes and therefore are prone to crack upon subsequent Li extraction and uptake. In this respect, the use of nanostructures and nanocomposites is a prerequisite to accommodate better the strains due to the electrochemical processes and to obtain longer cycle life for these negative electrodes [13–15].

Nanomaterials can also significantly improve charge transfer and power delivery in the electrodes because of larger surface contact with the electrolyte and shorter diffusion lengths for the charge carriers (i.e. Li^+ ions and electrons). In particular, the presence of small nanoparticles and extended interfaces is decisive in transition metal oxides to have almost fully reversible reactions [16,17], as well as extra charge storage at the boundaries in a pseudo-capacitive way [18,19]. Nevertheless, exploiting the features of nanomaterials in practical negative electrodes in most of the cases is not a trivial task. Their favourable characteristics can be easily masked by improper incorporation into the ultimate electrode structures. This holds especially when these materials are processed in a powder form and their dispersion and assembly in coated electrodes become more difficult. Various strategies have been proposed to address this issue. Nanoparticles finely dispersed in a supporting carbon matrix [20] or embedded in carbon microspheres [21–23], as well as carbon-encapsulated hollow structures [24], constitute elegant examples of fabrication of advanced negative electrodes. They result in significant improvement of the mechanical stability during cycling, preventing particle agglomeration and enhancing the electronic conductivity of the entire

* Corresponding author. Tel.: +31 0 15 2785536; fax: +31 0 15 2784945.
E-mail address: e.garciatamayo@tudelft.nl (E. García-Tamayo).

0378-7753/$ – see front matter © 2011 Elsevier B.V. All rights reserved.
doi:10.1016/j.jpowsour.2011.08.057

electrode. However, these methods generally require multi-step processes, which often involve the use of expensive precursors. Even in one-step syntheses, high temperatures (i.e. 700 °C) are usually necessary for the preparation of such nanocomposites. Moreover, the materials still need to be thoroughly mixed with a binder in a slurry and successively coated on a current collector.

Alternative methods for direct growth or deposition of active materials on current collectors are attractive to reduce the steps needed for electrode fabrication. For example, techniques such as electrodeposition [25], template-synthesis [26,27], physical vapour deposition [5], sputtering [28], vapour–solid–liquid (VLS) [29] or vapour–solid (VS) growth [30] have been widely used and interesting results have been obtained. In all these cases, binders and conductive additives (i.e. carbon black) are not included in the final electrodes. Nano-architectures (i.e. 3D self-supported nanowires or nanotubes arrays, etc.) are particularly attractive in terms of achievable capacities and rate capabilities, offering enhanced surface areas in contact with the electrolyte [31–33].

Rods, wires and especially tubes provide favourable geometries to accommodate the strain involved during uptake and removal of Li. In 3D nano-architectured electrodes each structure has its own contact with the substrate, contributing directly to the overall electrochemical reaction without any ancillary material needed for operation. However, the fabrication methods applied so far (i.e. template-assisted syntheses, VLS, VS, etc.) are quite cumbersome and, even in the most favourable cases, there are obvious limitations arising, for example, from pre-treatments needed for the substrates, the size of the template membranes, the use of expensive catalysts, the limited area coverage and the scarce amount of active material effectively grown. In this respect, template-free methods for spontaneous, large-area growth of self-standing nanowires arrays is very promising for a relatively cheap, easy and efficient preparation of advanced 3D nanostructured negative electrodes, involving only few process steps [34,35]. Still, this interesting approach may suffer from limited mechanical stability in practical battery assemblies. The risk of breaking the wires during the fabrication of the whole device should be also taken into account. Such circumstance results in a direct loss of capacity, since the electrical contact of the individual structures with the substrate is definitively lost. Therefore, the role of polymer binders and eventual additives in practical coated electrodes should not be overlooked, even though they account for inactive mass added to the entire structure. In this respect, an increasing number of studies are devoted to the investigation of various binders and their influence on the cycle performance of novel negative electrodes [36–40]. Active metal or metal-oxide nanoparticles need a suitable "glue" that holds them together and that reinforces the entire electrode during the electrochemical processes. Particles must adhere to the current collector and not move far apart from each other in order to ensure percolation. Additionally, the binder adhesion to the surface of the nanoparticles should be optimal, promoting the transport of the charge carriers to and from the particles, while preventing them from agglomeration and coalescence.

In this scenario, the possibility of direct synthesis and coating of nanocomposite layers, containing the active nanoparticles dispersed in a binder with eventual additives, is obviously attractive. More important, it is convenient to generate in situ the active nanoparticles already mixed with the binder, rather than dispersing them in a separate step. Indeed, the process of synthesis of the active materials does not need to be separated from their assembly in composite coated electrodes with other components.

Electrospray-based methods (i.e. electrospray pyrolysis & deposition, electrospinning) are powerful tools to perform such a one-step synthesis and coating of nanocomposite electrodes. Electrospray pyrolysis (ESP) and deposition (ESD), as well as electrospinning, have been widely applied to the preparation of thin films and functional materials [41,42]. Various thin-film positive and negative electrodes for Li-ion batteries [43–52] have been synthesized and deposited via ESP and ESD without any polymer binder. On the other hand, electrospinning has been used for the fabrication of composite polymer nanofibers, which are for example used to prepare membranes and separators [53–56], or carbonized in a separate step to yield carbon nanofibers loaded with active electrode materials [57,58]. However, in all these cases the polymers are *not* utilized for specific binding purposes in practical coated electrodes. A first attempt to utilize electrosprayed layers containing polymer binders for lithium ion battery electrodes was recently reported by our group [59]. In the present paper we concentrate on the process of electrospray pyrolysis of solutions containing precursor metal salts dissolved together with polyvinylidene fluoride (PVdF) binder. It is proposed that it is a viable approach to synthesize and assemble in one step thin nanocomposite coatings of negative electrodes at low temperature.

2. Experimental

2.1. Precursor solutions

Precursor solutions containing PVdF and different metal salts were prepared as follows. For a typical preparation ~0.1 g of PVdF powder (Solef) were added to ~10 mL of N-methyl-2-pyrrolidone (NMP – Merk-Schuchardt) and sealed in a glass bottle. Constant stirring was applied in order to dissolve the PVdF powder in NMP. Subsequently, an amount of approximately 0.5 g of the desired metal precursor salt, e.g. $SnCl_2{\cdot}2H_2O$ (Riedel-de Haën), or $Co(CH_3COO)_2{\cdot}4H_2O$ (Riedel-de Haën), or $Fe(CH_3COO)_2$ (Alpha), was added to the NMP–PVdF solution. Vigorous stirring was then applied in order to achieve complete dissolution of the salts. Different colors were obtained, depending on the type of the ions present in the solution.

2.2. Aerosol generation and electrode coating

All the experiments were performed in air and the deposition of the electrode layers was carried out inside a reaction chamber connected to a fume hood. A schematic drawing of the equipment used for the synthesis and assembly of the coated electrodes is shown in Fig. 1a.

The precursor solutions were transferred to a glass syringe (Fortuna Optima), which was connected through a chemically resistant hose (Watson-Marlow) to a stainless steel nozzle (EFD Ultra). The nozzle, on its turn, was connected to the positive pole of a high voltage power supply (HCN 14-12500). A syringe pump (Kd Scientific) enabled the feeding of the precursors to the nozzle at a controlled flow rate. The flow rate was tuned in the experiments in order to obtain stable electrospray conditions. Typical values were in the range of 0.20–0.40 mL h^{-1}. The voltage applied for the atomization was usually adjusted from about 8.0–10.0 kV, in order to obtain a homogeneous layer deposition, depending on the properties of the precursor solutions. The distance between the nozzle and the substrate was kept constant in all the experiments (i.e. 20 mm) and measured via a built-in digital calliper. The temperature of the substrate was set to 280 °C and was maintained constant by a thermostat during all the experiments. This temperature was high enough to obtain complete pyrolysis of the various precursors and quite far from the threshold for decomposition of PVdF in air (i.e. >315 °C). Possible pyrolysis reactions for the precursor salts are:

$$SnCl_2 \cdot 2H_2O + O_2 \xrightarrow{280\,^\circ C} SnO_2 + Cl_2\uparrow + 2H_2O\uparrow \quad (1)$$

$$Co(CH_3COO)_2 \cdot 4H_2O + 3O_2 \xrightarrow{280\,^\circ C} CoO + 2CO\uparrow + 2CO_2\uparrow + 7H_2O\uparrow \quad (2)$$

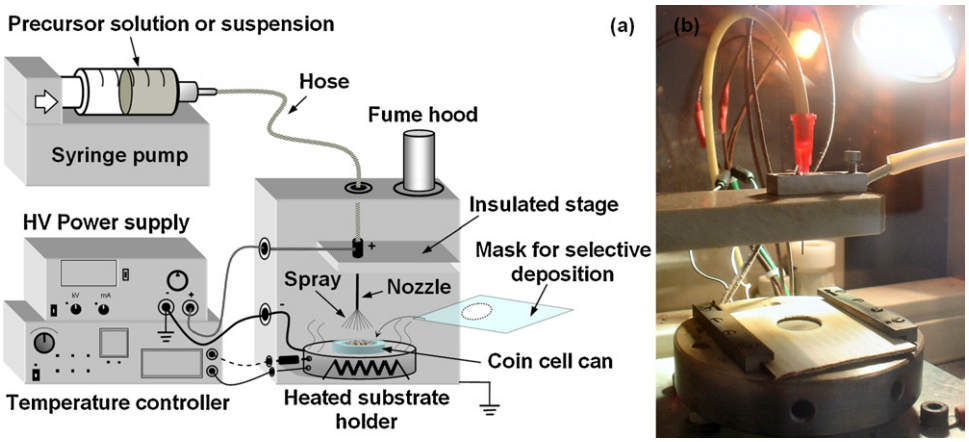

Fig. 1. Schematic drawing of the electrospray equipment used for the direct synthesis and coating of nanocomposite electrodes (a). Photo of the process of deposition in the reaction chamber (b). The electrified nozzle, the hot plate and the mask used to deposit circular electrode layers on coin cell cans are easily noticed in the photo.

$$2Fe(CH_3COO)_2 + 8O_2 \xrightarrow{280\,^{\circ}C} Fe_2O_3 + CO\uparrow + 7CO_2\uparrow + 6H_2O\uparrow \quad (3)$$

The weight percentage of the active oxide nanoparticles in the resulting composite electrodes was then calculated, giving approximately 76% for SnO_2, 60% for CoO and 69% for Fe_2O_3. In all the experiments a preliminary deposition was first performed on aluminium or stainless steel foil for easier characterization of the deposits. Analogous experimental conditions were then applied to achieve a selective electrode coating directly on coin cell cans. Empty stainless steel coin cell cans (CR2320 – Hohsen) were carefully weighted on a digital balance (Sartorius) with an accuracy of 10^{-5} g, before being mounted to the heated substrate holder. Selective coating on a circular area concentric to the rim of the coin cell can was achieved by applying a cardboard mask with a punched hole of ≈14 mm diameter. The hole of the mask was centered in the middle of the coin cell can. The mask and the can were held firmly together on the hot plate by two lateral supports (see Fig. 1b). After coating, the coin cell cans were weighted again and the amount of deposited composite material was determined by mass difference. The typical weight of the composite layers was around 0.8–1.2 mg. It should be pointed out that the coated electrodes did not need any further treatment and were directly sealed in a full coin cell assembly by adding the remaining parts. Carbon black was not included in the fabrication of the electrodes.

2.3. Characterization and electrochemical measurements

The produced materials were analyzed by different characterization techniques. X-ray diffraction (XRD) was performed on a Bruker (AXS D8 Advance) diffractometer equipped with a Cu Kα radiation source (λ = 1.5418 Å); Scanning Electron Microscopy (SEM) was carried out on a Philips XL20 microscope. Transmission Electron Microscopy (TEM) was also performed by two microscopes operated at 300 kV, namely Philips CM30T and FEI Tecnai F20, both equipped with a LINK EDX probe (Oxford) for elemental analysis. Furthermore, Atomic Force Microscopy (AFM) was carried out on a NT-MDT NTEGRA scanning probe microscope in semi-contact mode, using a Si cantilever and tip (NT-MDT, Silicon: NSG 03). The processed coin cell cans containing the deposited electrodes were assembled in complete cells in a He-filled glove-box (MBraun). The electrolyte consisted of 1 M $LiPF_6$ solution in EC:DMC (2:1 by wt. – Mitsubishi Chemicals) and metallic lithium disks were used as reference and counter electrodes for the electrochemical measurements. Galvanostatic tests were performed on a Maccor cycler (S-4000) at constant gravimetric current densities (i.e. 113 mA g^{-1} for SnO_2, 358 mA g^{-1} for CoO, 124 mA g^{-1} for Fe_2O_3). The cells were discharged and charged in different voltage ranges versus Li/Li^+, depending on the electrode materials. Specimens for TEM 'post mortem' analysis of the cycled materials were prepared and collected inside the glove-box, where the coin cells were disassembled. The electrodes were washed thoroughly by EC in order to remove completely the electrolyte salt before collecting the samples for the analysis.

3. Results and discussion

Fig. 2 shows some photos of the different nanocomposite electrodes deposited on coin cell cans. It is seen that the resulting coatings are fairly homogeneous and their colors indicate that different metal oxide particles inter-dispersed within PVdF have been formed. Indeed, the faint white-yellowish (a), black (b) and dark reddish-brown (c) hues match with the characteristic colors of the oxide produced (i.e. SnO_2, CoO and Fe_2O_3).

The local surface morphology of the different electrodes is presented in Fig. 3, where their AFM micrographs are shown. It can be observed that in all the cases sub-micrometric deposits have been formed from the reacted droplets generated during electrospraying. Their typical size varies from tens of nanometres to roughly 300 nm. It is worth noticing that all the deposits have a spherical-like shape, indicating that most of the evaporation of the solvent (i.e. NMP) and the precursor decomposition in the generated droplets practically occurred during their flight towards the heated substrate [41].

In this respect, each charged droplet acts as a sort of 'microreactor' for the formation of the ultimate materials. The spherical features are particularly pronounced for the CoO/PVdF and Fe_2O_3/PVdF deposits, shown in Fig. 3b and c respectively, while the SnO_2/PVdF remnants (Fig. 3a) display less regular contours and a cluster-like shape.

The nanocomposite electrode layers were analyzed by XRD to investigate the structure of the synthesized materials. Fig. 4 shows the different diffraction patterns obtained for SnO_2/PVdF (a), CoO/PVdF (b) and Fe_2O_3/PVdF (c) respectively.

The sharp peaks present in the spectra are due to the underlying supports, i.e. Al (Fig. 4a and b) and stainless steel (Fig. 4c) and no distinctive diffractions related to the various metal oxide structures are detected. Hence, the resulting metal oxide particles exhibit mainly amorphous-like features, as it can be expected for their synthesis at low temperature. Moreover, the presence of small nanoparticles results in extensive broadening of eventual diffractions. Indeed, the pattern of Fig. 4a displays broad diffractions around 27° and 52°, which are generally observed in the

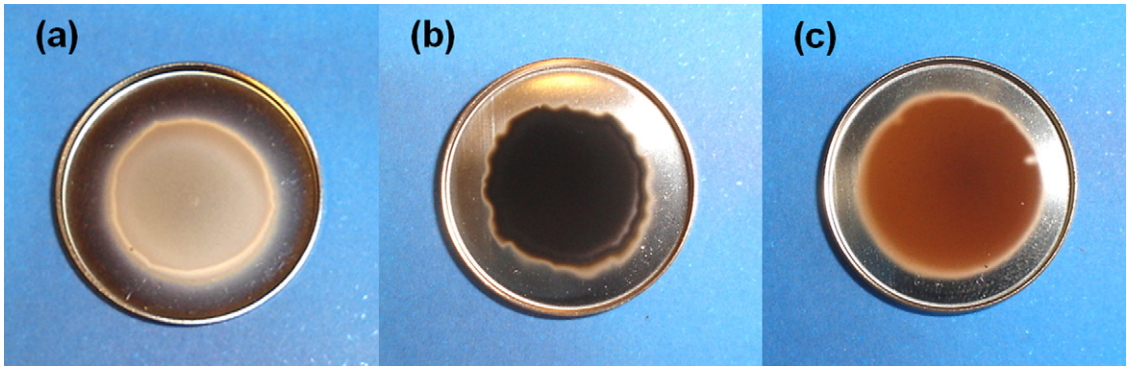

Fig. 2. Photos of the different nanocomposite electrodes directly deposited on coin cell cans by electrospray pyrolysis of various precursors at 280 °C. SnO_2/PVdF (a), CoO/PVdF (b) and Fe_2O_3/PVdF (c) electrodes.

presence of nanocrystalline SnO_2 [60], even though reports on electrospray pyrolysis of $SnCl_2{\cdot}2H_2O$ solutions at 250 °C in air suggest that amorphous SnO_2 is usually formed [61]. Conversely, the spectrum in Fig. 4b shows that the synthesized material is completely amorphous, as expected for spray pyrolysis of cobalt acetate solutions in air at low temperatures. Previous investigations reveal the formation of a 'low-temperature' (i.e. 240–400 °C) pure CoO phase [46,62,63], which transforms into Co_3O_4 only at higher temperatures. Fig. 4c shows that also electrospray pyrolysis of iron acetate resulted in the formation of amorphous Fe_2O_3, since only a slight bump around 33° is detected, in correspondence of the angular range where the strongest diffractions of Fe_2O_3 occur.

TEM analysis was then performed in order to shed light on the intimate structure of the composite deposits and their texture. Fig. 5 shows various images of the nanocomposites SnO_2/PVdF (a and a′), CoO/PVdF (b and b′) and Fe_2O_3/PVdF (c and c′).

From Fig. 5a–c, it can be seen that the typical size of the remnants varies roughly from 20 nm up to 300 nm, matching well with the previous AFM analysis. The shape of the remnants proves that the generated materials are reminiscent of the

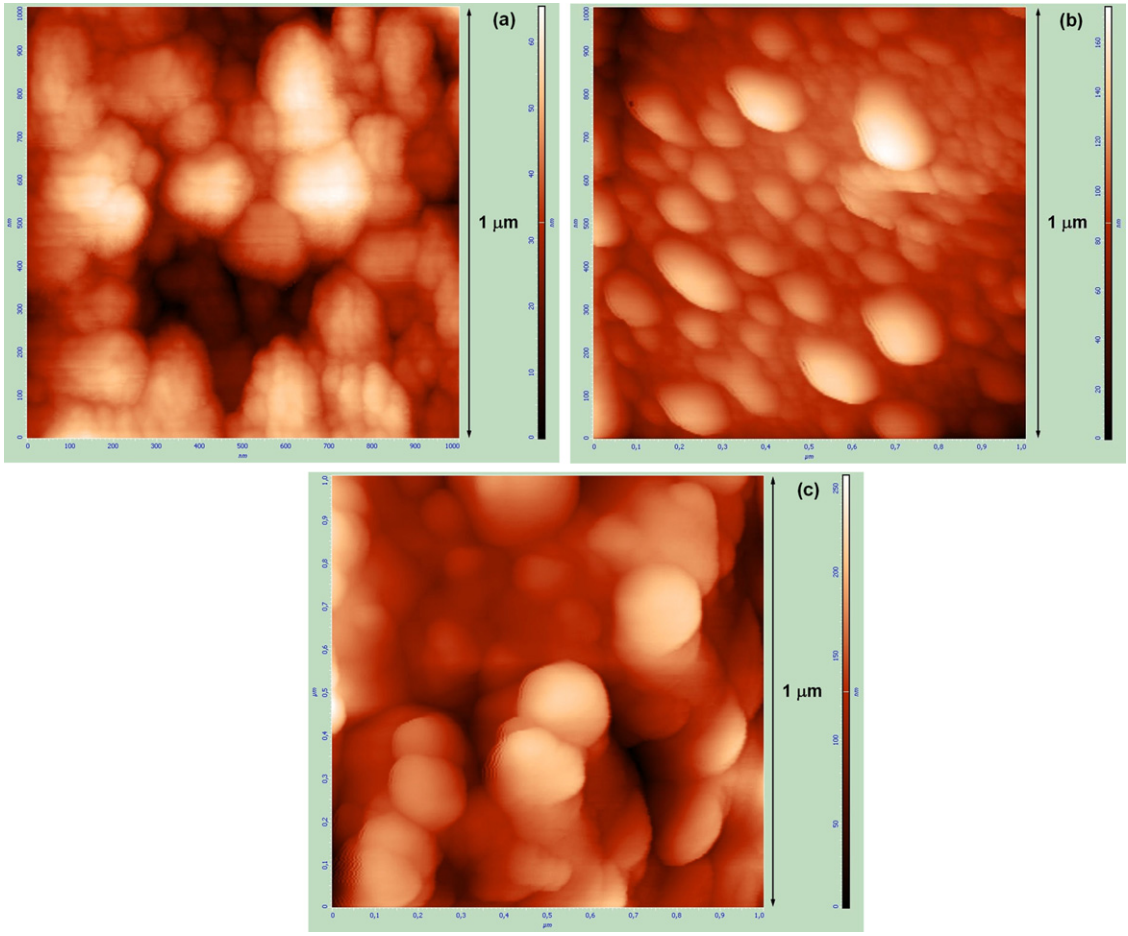

Fig. 3. AFM images of the characteristic surface morphologies of the various nanocomposite electrodes obtained by electrospray pyrolysis at 280 °C. SnO_2/PVdF (a), CoO/PVdF (b) and Fe_2O_3/PVdF (c). The scanned areas in all the samples are 1 μm × 1 μm.

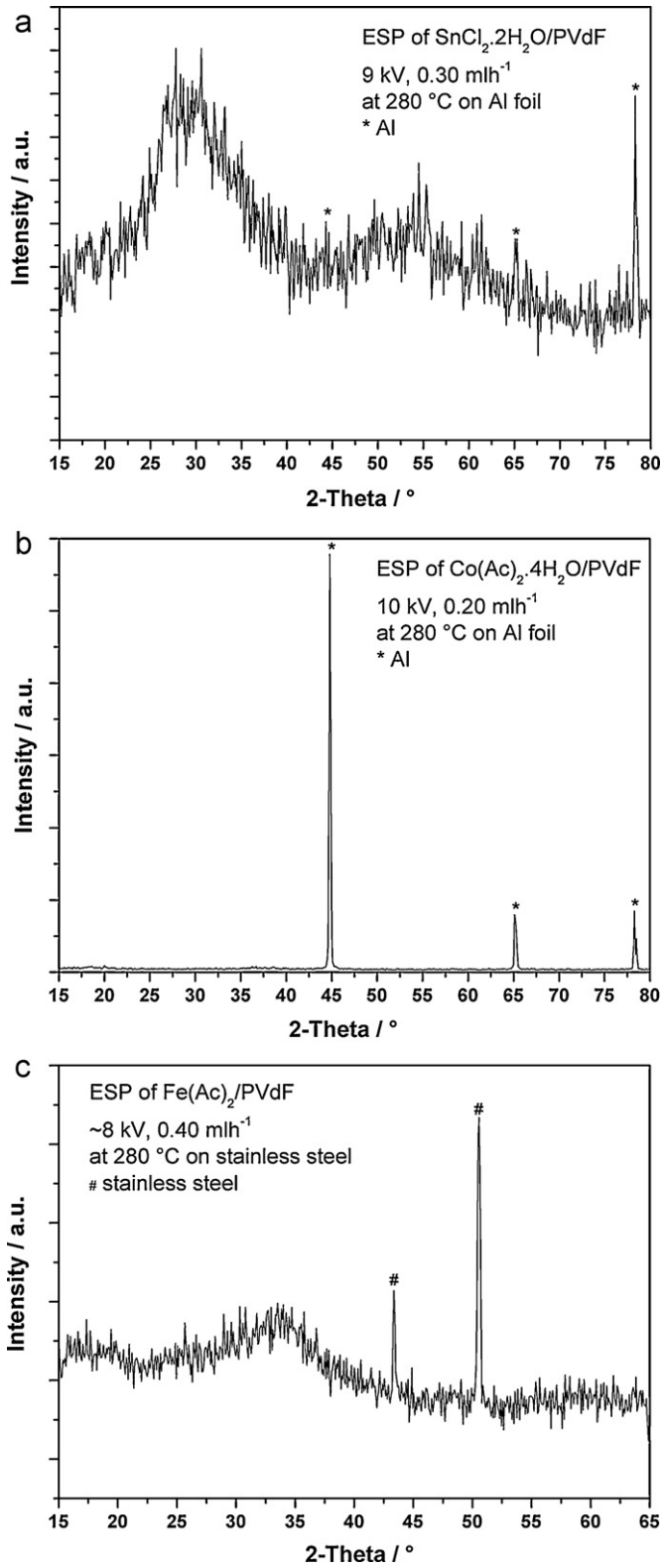

Fig. 4. XRD patterns of the various nanocomposite electrode layers deposited by electrospray pyrolysis at 280 °C. SnO_2/PVdF (a) and CoO/PVdF (b) layers on Al foil. Fe_2O_3/PVdF (c) on stainless steel. Note that the sharp peaks in the spectra correspond to the characteristic reflections of the underlying supports (i.e. Al or stainless steel).

electro-evaporation processes, as immediately seen for the spherical Fe_2O_3/PVdF deposits in Fig. 5c. The micrographs at higher magnification reveal that small nanoparticles of few nanometers (see dotted circles) have been formed and evenly inter-dispersed within PVdF (see arrows) in all the conglomerated relics of the droplets from the various precursors. In particular, nanocrystals of SnO_2 of about 2–5 nm are observed throughout the agglomerate in Fig. 5a′ and their characteristic lattice fringes clarify the previous XRD pattern of Fig. 4a. On the other hand, the nanoparticles made of CoO (Fig. 5b′) and Fe_2O_3 (Fig. 5c′) do not display any sign of lattice fringes and their typical size is approximately in the range of 1–10 nm. The amorphous character of the CoO nanoparticles is further confirmed by Selected Area Electron Diffraction (see inset of Fig. 5b) that shows only a diffused pattern with some faint rings, where no diffraction dots are observed. It is important to note that PVdF surrounds the particles in all the various nanocomposites in Fig. 5, thus reinforcing the nanostructured material at a local nanometric level, while enhancing mutual adhesion of the deposits and improving the overall contact with the substrate at a macroscopic scale. At the same time, it can be expected that pores have been produced in the remnants during the processes of evaporation and pyrolysis, as it appears from the TEM micrographs. Porosity is particularly important in this type of electrodes, because apart from allowing direct access of the electrolyte to the active materials, it provides free space that can accommodate volume variations. Besides, the amorphous nanostructures undergo isotropic expansion and contraction upon electrochemical cycling [64] and this circumstance helps the binder immobilizing the particles and preserving the integrity of the electrodes. These characteristics, as well as the pronounced presence of lattice defects, can significantly contribute to improve cycleability, as well as Li^+ transport and storage in the electrodes. Extended interfaces, as well as curved surfaces, are ultimately responsible for other thermodynamical effects [65]. In this case, the PVdF layer that surrounds both the individual nanoparticles and the whole deposit is expected to exert an action similar to that of a 'balloon' at both characteristic scales. On the one hand, it prevents agglomeration and coalescence of the nanoparticles, on the other hand it helps holding the nanoparticles tight within the deposits, while buffering their volume changes upon cycling. It is important to mention that the grain size of the particles can be controlled by tuning the properties of the precursor solution and/or by changing the experimental parameters (i.e. flow rate, voltage, temperature, etc.).

The electrochemical analysis of the various nanocomposites is here discussed separately for each electrode. Fig. 6 shows the results for the galvanostatic test carried out on the SnO_2/PVdF electrode cycled between 0.05 and 1.2 V.

The first discharge in Fig. 6a yields a capacity of about 180 mAh g^{-1}, likely due to the reactive surface area and the presence of lattice defects. Indeed, a remarkable amount of Li is irreversibly consumed in the formation of the SEI layer and in the conversion reaction of the oxide, according to the general mechanism [66]:

$$2xLi^+ + 2xe^- + SnO_x \rightarrow xLi_2O + Sn \quad \text{with } 1 \le x \le 2 \tag{4}$$

$$yLi^+ + ye^- + Sn \leftrightarrow Li_ySn \quad \text{with } 0 < y \le 4.4 \tag{5}$$

After the first charge up to 1.2 V, the recovered capacity is about one third of the initial value, which is in line with the poor reversibility exhibited by SnO_2. No definite plateaus are displayed in the first discharge and only a slight bump is detected around 0.8 V. Overall, slopy discharge–charge curves are observed in Fig. 6a, suggesting that under these conditions the reactions in Eqs. (4)–(5) take place in a way where the formation of a sort of 'solid solution' in the nanocrystalline material is favoured to phase segregation. The capacity of the second discharge and charge exceed that of the

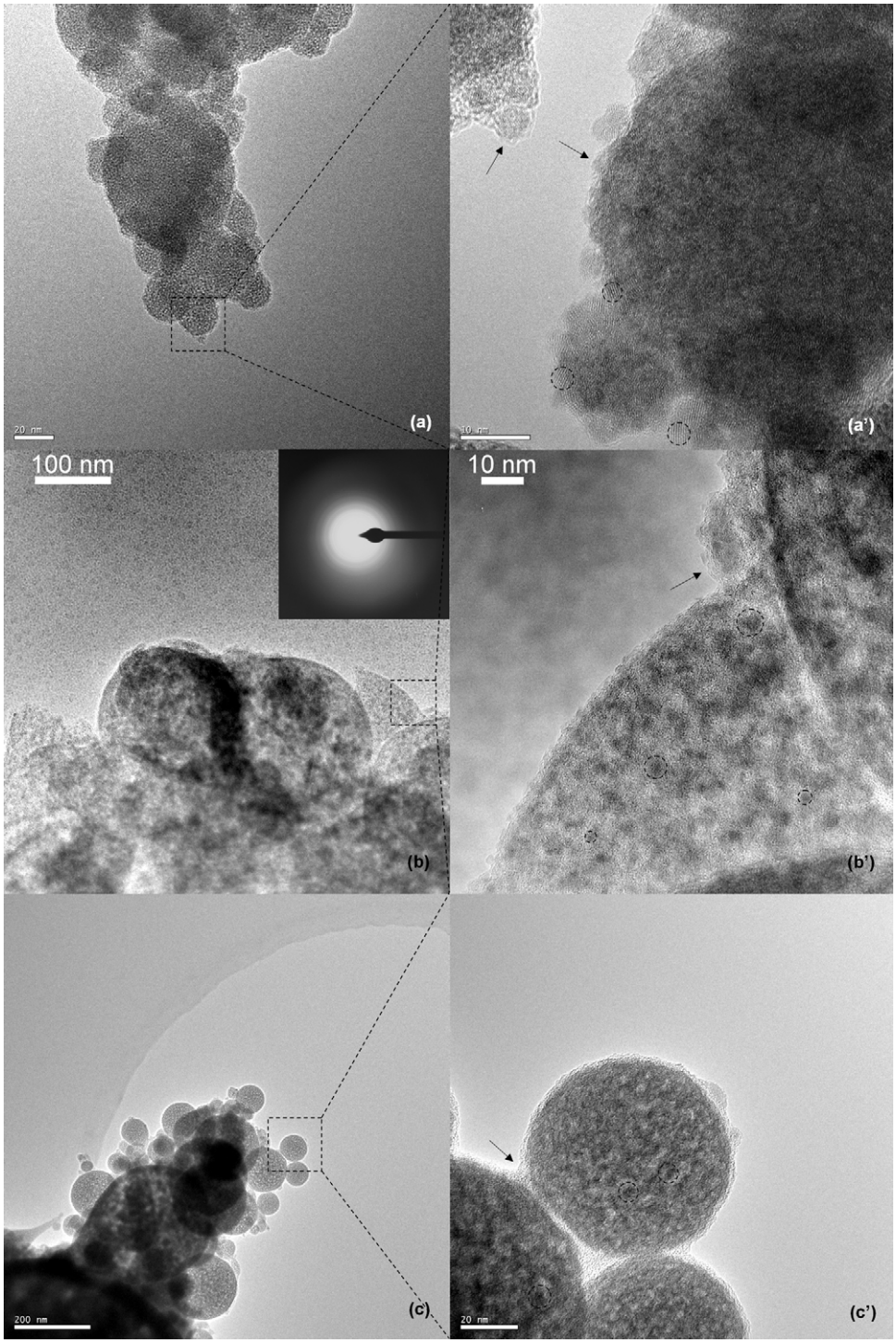

Fig. 5. TEM micrographs at different magnifications of the various nanocomposites synthesized by electrospray pyrolysis at 280 °C. Images of SnO_2/PVdF (a and a′). Images of CoO/PVdF (b and b′), where the inset in (b) shows the corresponding SAED. Images of Fe_2O_3/PVdF (c and c′). Note that the arrows highlight the PVdF layer in all close up images of the composites, while the dotted circles enclose some individual nanoparticles of the respective metal oxides.

first charge, indicating that a sort of activation of the nanoparticles occurs after the first cycle. Consequently, a small rise in capacity is seen for the first four charges in the plot of the cycle performance (Fig. 6b). Despite the initial capacity loss, the nanocomposite SnO_2/PVdF performed quite well during the following cycles, yielding a reversible capacity of 580 mAh g^{-1} after 50 cycles.

It is noteworthy to mention that the electrode was able to cycle without *any* conductive additive, notwithstanding SnO_2 is a semiconductor and PVdF an insulator. The slight fading of the capacity after the first twenty cycles in Fig. 6b can be likely due to a limited electronic conductivity and a progressive thickening of the SEI layer formed during the first cycles. However, the main issue of Sn-based materials is represented by their poor mechanical stability. The severe volume change of the Sn host (i.e. up to 256%) upon reaction with Li (see Eq. (5)) usually damages the electrode after a few cycles when bulk materials are employed. Here the converted Sn nanoparticles inhibit cracking and crumbling of the host material, nonetheless the whole composite is subjected to remarkable strain.

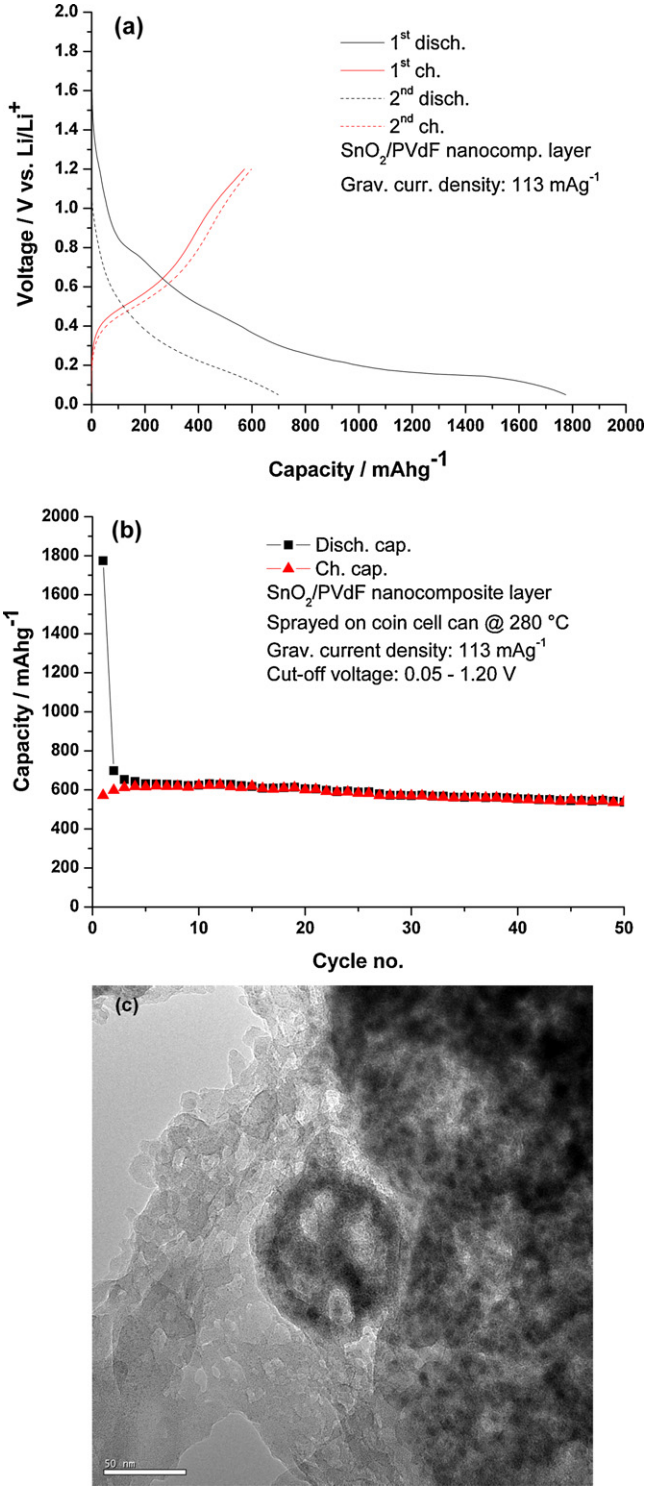

Fig. 6. Voltage profile of the SnO_2/PVdF nanocomposite electrode for the first two cycles of discharge–charge (a). Cycle performance of the same electrode (b). TEM image of 'post-mortem' analysis of the tested electrode after 50 cycles (c).

Indeed, the mechanical properties of PVdF are seriously challenged by repeated extension and contraction of the electrode [38], as well as by eventual loss of adhesion to the surface of the particles, due their shape change upon charge and discharge. Therefore, these circumstances progressively deteriorate the capacity retention of the electrodes. From Fig. 6b it can be inferred that the mechanical stability of the nanocomposite electrode is quite good and that the process of fabrication enhanced the adhesion of PVdF, as well as the homogeneous dispersion of the active SnO_2 nanocrystals. TEM 'post mortem' analysis of the electrode after 50 cycles of discharge and charge supports these hypotheses. The micrograph in Fig. 6c shows particles whose size is larger than that of the original nanocrystals. However, their size is below 20 nm and the PVdF still surrounds the particles, preventing the Sn nanoparticles from growing into larger agglomerates, which are prone to undergo cracking. It is seen that the individual particles are not damaged by the cycling and that, regardless of the increase in size, they retained their structural integrity. Interestingly, the remnant in the middle of Fig. 6c has not broken apart and has maintained its shape along with its nanostructured features, despite some distortion.

Fig. 7 presents the results of the galvanostatic test of the CoO/PVdF electrode cycled between 0.05 and 3.0 V.

The first discharge curve in Fig. 7a shows a long plateau around 1.1 V after an initial voltage drop. The plateau is then followed by a tail ending at 0.05 V. This plateau corresponds to the generation of SEI layer around the nanoparticles and their conversion to metallic Co and Li_2O, according to the general reaction:

$$M_xO_y + 2yLi^+ + 2ye^- \leftrightarrow yLi_2O + xM^0 \quad (6)$$

where M represents the transition metal (e.g. Co, Fe, Cu, Ni, Ru, etc.) of interest.

It is worth noticing that here the reaction accounts for a capacity larger than 1000 mAh g^{-1}. The theoretical capacity of CoO is 716 mAh g^{-1}, still the large contribution of the plateau is not surprising, considering the large surface area of the nanostructured CoO and the peculiar texture of the deposits (see Fig. 5b and b′). Furthermore, the tail is responsible for a final capacity that reaches 1670 mAh g^{-1}. This part of the curve corresponds to extra storage of Li^+ and e^- in the respective neighbouring Li_2O and Co nano-phases [16,18,67]. The reduced size of the pristine CoO nanoparticles is expected to strengthen this phenomenon, since it enhances the interfacial area. However, the extended reactive surface area is also detrimental for the initial reversibility of the electrode, leading to irreversible trapping of Li in the early stage of SEI formation. In fact, the first charge up to 3.0 V in Fig. 7a yields a capacity of about 1240 mAh g^{-1}, which corresponds approximately to a coulombic efficiency of 74%. The steep part of the charge curve, starting at 0.05 V and bending at 1.1 V, corresponds roughly to the extraction of the interfacial charge, while the following part up to 1.9 V is associated to the decomposition of the SEI layer [68]. The full regeneration of CoO then takes place between 1.9 and 3.0 V. A small shoulder around 2.2 V is detected at the beginning of the second discharge (see arrow in Fig. 7a). This feature has been previously observed and attributed to the intercalation of Li^+ into a small fraction of newly formed $LiCoO_2$ [68]. Indeed, it has been demonstrated that a small amount of $LiCoO_2$ can be spontaneously formed in the presence of CoO, Li^+ and $(CO_3)^{2-}$ [69,70]. Another prominent feature in the second discharge is the flat plateau rising at 1.3 V. This rise in potential is an intrinsic characteristic related to the initial conversion of the CoO and its pulverization in the following cycles. In fact, after the initial decomposition into Co^0 and Li_2O in the first discharge, only nanoparticles of 1–2 nm are left [6]. The regenerated CoO particles then should have a similar size. Hence, an initial reduction of the size of the pristine particles occurs here as well. The result is that upon reaction with Li in the second discharge these CoO nanoparticles are pulverized and their surface energy is decreased due to interaction with the produced Li_2O [23,71]. The discharge curve then displays a slant segment up to 0.6 V, which is followed by a tail, as in the first discharge. The following charge curve does not differ from the first one, apart from some minor capacity loss. The subsequent cycles result also in activation of the material, as it can be noticed from the plot of cycle performance in Fig. 7b.

Despite the irreversible capacity loss in the first cycle, a steady increase of the capacity is observed after the third cycle up to cycle

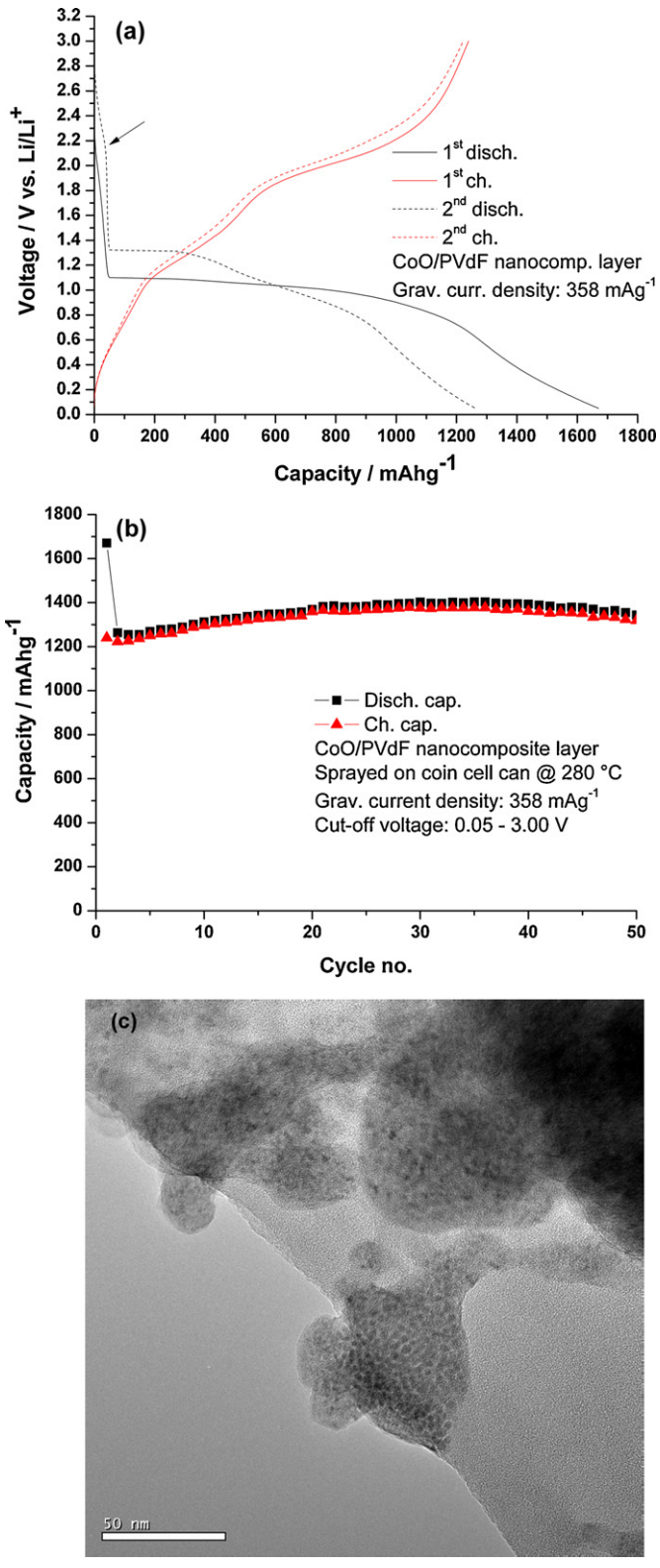

Fig. 7. Voltage profile of the CoO/PVdF nanocomposite electrode for the first two cycles of discharge–charge (a). Cycle performance of the same electrode (b). TEM image of 'post-mortem' analysis of the tested electrode after 50 cycles (c).

number 36. This rise in capacity has been previously described as an 'activation period' [68], where for small current densities this increase has been found up to cycle 22. From Fig. 7b it is seen that the correspondent discharge capacity at the 36th cycle reaches 1400 mAh g^{-1}. However, this value is still lower than that of the first discharge. Therefore, it can be concluded that even though the activation period enabled the release of lithium from some irreversible Li_2O generated during the first cycle, a certain amount of Li^+ is lost in the initial reaction, due to the SEI formation and irreversible trapping by eventual impurities. After the 36th cycle a slight decrease of the performances occurs. The final discharge capacity after 50 cycles drops to 1350 mAh g^{-1}, which is still more than three times and a half the theoretical value for the graphite. Once again, it is remarkable that such a result has been obtained without any conductive additive and with PVdF as binder. Indeed, the homogeneous formation of extremely small Co^0 dots facilitates efficient transport of the electrons through the electrode, while the neighbouring Li_2O nano-phase enables reversible storage and transport of Li^+. Nevertheless, the mechanical strain that the electrode undergoes upon repeated cycling should not be overlooked. Uptake and removal of Li in CoO causes a theoretical volume change of about 52%, which still needs to be accommodated by the binder. Clearly the volume variation of CoO is about five times lower than that of Sn and this fact, together with the structure and texture of the nanocomposite, contributes to its optimal cycling performance. TEM 'post mortem' analysis of the electrode after 50 cycles confirmed again that the fabrication process was effective in preserving the structural properties of the nanocomposite. The nanoparticles are clearly separated from each other in Fig. 7c and their typical size is roughly 5 nm. The binder surrounds the particles and hindered their aggregation. Moreover, the reacted relics, even though distorted, maintained their integrity.

The results of the galvanostatic test for the Fe_2O_3/PVdF electrode, cycled between 0.05 and 3.0 V, are presented in Fig. 8.

The first discharge curve in Fig. 8a displays an initial sloping part, followed by a plateau around 0.9 V, corresponding to the conversion of the iron oxide. A tail is also observed at lower voltages ending at 0.05 V. The first discharge capacity is about 1030 mAh g^{-1}, while the first charge up to 3.0 V yields almost 700 mAh g^{-1}, corresponding to a coulombic efficiency of approximately 68%. A certain loss of reversibility is visible in the subsequent discharge and charge curves, which shift towards lower capacities, maintaining profiles similar to those of the first cycle. Interestingly, no rise in the potential of the 'conversion plateau' is detected in the second discharge, indicating that the process of reaction with lithium is somehow different from that of CoO. Indeed, the particles of Fe_2O_3 are not directly decomposed upon reaction with lithium, while the initial formation of an intermediate $Li_xFe_2O_3$ compound has been reported [72]. The evolution of charge and discharge capacities upon repeated cycling is shown in Fig. 8b. The capacity fading is particularly evident in the first five cycles, which account for a slump to about 600 mAh g^{-1}. Despite that, after 50 cycles the final capacity is approximately 515 mAh g^{-1}. Therefore, this electrode mainly suffers from capacity loss in the first cycles and no activation of the nanoparticles has been observed, suggesting that the formation and subsequent thickening of the SEI layer does not enable efficient charge transfer at the surface of the active material. The following cycles bring about only a moderate fading. The complete conversion of Fe_2O_3 to form $2Fe^0$ and $3Li_2O$ according to the general Eq. (6) causes a theoretical volume change of 93%, which needs to be sustained by PVdF and causes significant strain. Besides, the insulating properties of PVdF hamper efficient charge transport for Fe_2O_3, which is a poor electron conductor, especially when compared to other transition metal oxides, as, for example, RuO_2. In this respect, the effective transfer of electrons to and within Fe_2O_3 nanomaterials has been addressed in previous studies, showing that it is of utmost importance for sustaining high current densities and that it constitutes the rate limiting factor [73]. The reduction in size of the active particles in this case is only a pre-requisite to increase the performances of the nanocomposite. Still, it is not sufficient, since also the requirement of efficient electron/ion transport

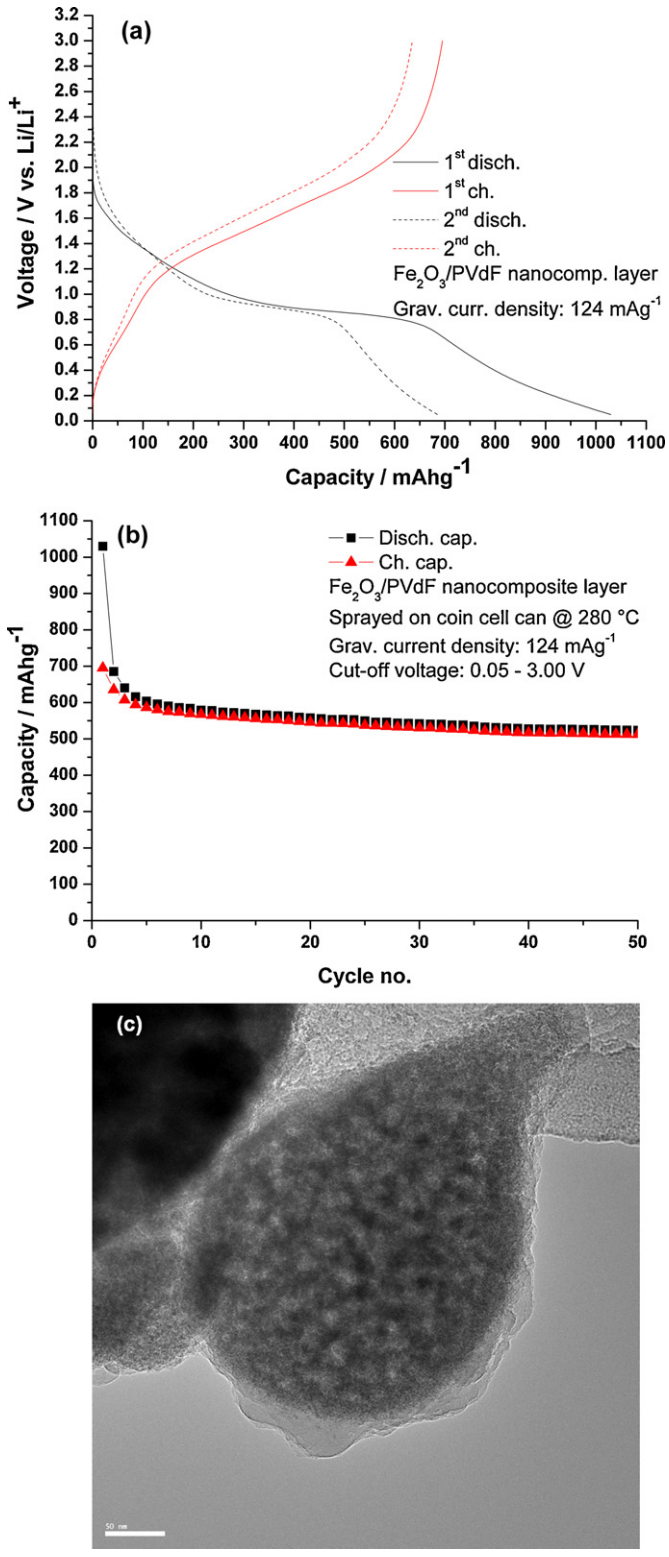

Fig. 8. Voltage profile of the Fe2O3/PVdF nanocomposite electrode for the first two cycles of discharge–charge (a). Cycle performance of the same electrode (b). TEM image of 'post-mortem' analysis of the tested electrode after 50 cycles (c).

in the major steps of the kinetics (i.e. electron and ion transport from their 'reservoirs' to the active particles, charge incorporation through their surface and transfer of the Li component inside their solid structure) of composite electrodes should be met [74]. 'Post mortem' analysis of the electrode was then performed by TEM in order to investigate the effects of the electrochemical cycling. Fig. 8c shows a micrograph of the Fe_2O_3/PVdF after 50 cycles. The image reveals that the nanocomposite relics are not destroyed by the cycling. The nanoparticles are enclosed in the composite remnant, which preserved its spherical shape and its characteristic texture and porosity. It is interesting to see that the particles are not damaged, despite a certain growth in size. They are in close contact and this fact further supports the idea that here the main hurdle for Fe_2O_3 nanoparticles is represented by their scarce electrical conductivity and limited electron transfer at the interfaces of the composite electrode. From Fig. 8c it is also seen that the remnant is covered by a thick surface layer that is probably due to the SEI formation and growth, which further hinders the electronic conduction to and from the nanoparticles. Therefore, it can be concluded that the Fe_2O_3/PVdF nanocomposite cycled relatively well, especially if the intrinsic limitation arising from the poor electrical properties of the oxide and the complete absence of conductive additives to promote the conduction among the composite structures are taken into account. In particular, the possibility of having a carbon coating or filler in this preparation could lead to a significant improvement of the performances of this attractive material, which is cheap, abundant and non-toxic.

4. Conclusions

An easy, cost-effective approach for the direct synthesis and coating of advanced nanocomposite negative electrodes at low temperature has been presented. This one-step method, based on electrospray pyrolysis in air of precursor solutions containing metal salts and PVdF binder dissolved together, enables the formation and deposition of metal oxide/PVdF nanocomposites, whose characteristics can be tuned by controlling the experimental conditions. Needless to say that various products, with desired compositions, thicknesses, morphologies and textures can be obtained by using dedicated precursors, solvents, polymers, additives, gas atmospheres and so forth. The method combines the powerful aerosol tool of electrospray deposition (i.e. generation of highly charged droplets with tuneable size, large area coverage, etc.) with the intrinsic versatility of wet chemistry and polymers, in order to form nanocomposite functional materials with peculiar structures and textures. Embracing in a single step the various stages required by conventional electrode preparation (i.e. blending of slurries, paste casting and coating consolidation) is extremely useful and effective in minimizing time and energy needed for electrode fabrication. Even more important is the fact that the active nanoparticles are generated in situ, while being inter-dispersed with the polymer binder and directly attached to the substrate, thus not separating the processes of materials synthesis, mixing and assembly. Moreover, the control over the morphology, the coverage and the thickness of the coatings by electrospraying can be controlled in a more accurate manner than in conventional laminated electrodes. Obviously, all these features are attractive not only for the fabrication of electrodes for Li-ion batteries, but also for other applications that may require deposition of functional nanocomposite structures. The initial results obtained for the synthesis of SnO_2, CoO and Fe_2O_3 nanocomposite electrodes are quite promising. Despite the intrinsic hurdles related to these materials and the limited mechanical properties of PVdF, this approach clearly shows the impact of the fabrication for this type of negative electrodes. The excellent cycling of CoO/PVdF in absence of any conductive additive suggests that the favourable properties of this material can be fully exploited by proper fabrication of nanostructured composites. In this way, its electrochemical performances can be even boosted by enhancing the contribution of interfacial charge storage phenomena occurring at the nanoscale. The performances of SnO_2/PVdF and Fe_2O_3/PVdF are not optimal and certainly they

can be improved. Still they indicate that this approach was successful in enhancing their mechanical properties and maintaining the integrity of the materials upon cyclying. It is important to mention that the presented method can be extended to the fabrication of other electrode materials by changing, for example, gas atmosphere and precursors. It is possible to produce not only oxides, but also metals, specifically for negative electrodes, since positive electrodes usually require higher temperature regimes, where the polymer binder is no longer stable.

Finally, it should be mentioned that this procedure, which has been carried out here on a lab scale (i.e. deposition on coin cell cans), has the potential to be implemented into a continuous, larger scale process for full fabrication of advanced nanocomposite electrodes in a roll-to-roll process by convenient outscaling of electrospray via multiple nozzle systems or equivalent equipments.

Acknowledgements

The authors acknowledge the European Research Institute ALISTORE-ERI, the Dutch Ministry for Economic Affairs via Agentschap NL and the EC via the E-stars project (ICT-223927) for funding the programme for nanomaterials syntheses. David Munaó, Corrado Locati, Caner Yurteri and Patricia Kooijman are gratefully acknowledged for their valuable help, collaboration and technical assistance.

References

[1] J.O. Besenhard, J. Yang, M. Winter, Journal of Power Sources 68 (1) (1997) 87–90.
[2] M. Winter, J.O. Besenhard, Electrochimica Acta 45 (1) (1999) 31–50.
[3] R.A. Huggins, Journal of Power Sources 81–82 (1999) 13–19.
[4] Y. Idota, T. Kubota, A. Matsufuji, Y. Maekawa, T. Miyasaka, Science 276 (5317) (1997) 1395–1397.
[5] J. Graetz, C.C. Ahn, R. Yazami, B. Fultz, Electrochemical and Solid-State Letters 6 (9) (2003).
[6] P. Poizot, S. Laruelle, S. Grugeon, L. Dupont, J.M. Tarascon, Nature 407 (6803) (2000) 496–499.
[7] P. Poizot, S. Laruelle, S. Grugeon, J.M. Tarascon, Journal of the Electrochemical Society 149 (9) (2002).
[8] J. Yang, M. Wachtler, M. Winter, J.O. Besenhard, Electrochemical and Solid-State Letters 2 (2–4) (1999) 161–163.
[9] J. Yang, Y. Takeda, N. Imanishi, J.Y. Xie, O. Yamamoto, Solid State Ionics 133 (3) (2000) 189–194.
[10] M.N. Obrovac, L. Christensen, D.B. Le, J.R. Dahn, Journal of the Electrochemical Society 154 (9) (2007).
[11] P.G. Bruce, B. Scrosati, J.M. Tarascon, Angewandte Chemie – International Edition 47 (16) (2008) 2930–2946.
[12] H. Liu, G. Wang, J. Wang, D. Wexler, Electrochemistry Communications 10 (12) (2008) 1879–1882.
[13] Y.G. Guo, J.S. Hu, L.J. Wan, Advanced Materials 20 (23) (2008) 2878–2887.
[14] A. Trifonova, M. Wachtler, M.R. Wagner, H. Schroettner, C. Mitterbauer, F. Hofer, K.C. Moller, M. Winter, J.O. Besenhard, Solid State Ionics 168 (1–2) (2004) 51–59.
[15] A.S. Arico', P. Bruce, B. Scrosati, J.M. Tarascon, W. Van Schalkwijk, Nature Materials 4 (5) (2005) 366–377.
[16] P. Balaya, H. Li, L. Kienle, J. Maier, Advanced Functional Materials 13 (8) (2003) 621–625.
[17] J. Maier, Nature Materials 4 (11) (2005) 805–815.
[18] J. Jamnik, J. Maier, Physical Chemistry Chemical Physics 5 (23) (2003) 5215–5220.
[19] P. Balaya, A.J. Bhattacharyya, J. Jamnik, Y.F. Zhukovskii, E.A. Kotomin, J. Maier, Journal of Power Sources 159 (1 (spec. iss.)) (2006) 171–178.
[20] G. Derrien, J. Hassoun, S. Panero, B. Scrosati, Advanced Materials 19 (17) (2007) 2336–2340.
[21] R. Demir Cakan, M.M. Titirici, M. Antonietti, G. Cui, J. Maier, Y.S. Hu, Chemical Communications (32) (2008) 3759–3761.
[22] R. Demir-Cakan, Y.S. Hu, M. Antonietti, J. Maier, M.M. Titirici, Chemistry of Materials 20 (4) (2008) 1227–1229.
[23] R. Yang, Z. Wang, J. Liu, L. Chen, Electrochemical and Solid-State Letters 7 (12) (2004).
[24] G. Cui, Y.S. Hu, L. Zhi, D. Wu, I. Lieberwirth, J. Maier, K. Mullen, Small 3 (12) (2007) 2066–2069.
[25] S.T. Chang, I.C. Leo, C.L. Liao, J.H. Yen, M.H. Hon, Journal of Materials Chemistry 14 (12) (2004) 1821–1826.
[26] N. Li, C.R. Martin, Journal of the Electrochemical Society 148 (2) (2001).
[27] N. Li, C.R. Martin, B. Scrosati, Electrochemical and Solid-State Letters 3 (7) (2000) 316–318.
[28] L.Y. Beaulieu, T.D. Hatchard, A. Bonakdarpour, M.D. Fleischauer, J.R. Dahn, Journal of the Electrochemical Society 150 (11) (2003).
[29] C.K. Chan, X.F. Zhang, Y. Cui, Nano Letters 8 (1) (2008) 307–309.
[30] C.K. Chan, R. Ruffo, S.S. Hong, Y. Cui, Journal of Power Sources 189 (2) (2009) 1132–1140.
[31] L. Bazin, S. Mitra, P.L. Taberna, P. Poizot, M. Gressier, M.J. Menu, A. Barnabe', P. Simon, J.M. Tarascon, Journal of Power Sources 188 (2) (2009) 578–582.
[32] P.L. Taberna, S. Mitra, P. Poizot, P. Simon, J.M. Tarascon, Nature Materials 5 (7) (2006) 567–573.
[33] C.K. Chan, H. Peng, G. Liu, K. McIlwrath, X.F. Zhang, R.A. Huggins, Y. Cui, Nature Nanotechnology 3 (1) (2008) 31–35.
[34] Y. Li, B. Tan, Y. Wu, Journal of the American Chemical Society 128 (44) (2006) 14258–14259.
[35] Y. Li, B. Tan, Y. Wu, Nano Letters 8 (1) (2008) 265–270.
[36] J. Li, L. Christensen, M.N. Obrovac, K.C. Hewitt, J.R. Dahn, Journal of the Electrochemical Society 155 (3) (2008).
[37] J. Li, R.B. Lewis, J.R. Dahn, Electrochemical and Solid-State Letters 10 (2) (2007).
[38] Z. Chen, L. Christensen, J.R. Dahn, Journal of Applied Polymer Science 90 (7) (2003) 1891–1899.
[39] Z. Chen, L. Christensen, J.R. Dahn, Electrochemistry Communications 5 (11) (2003) 919–923.
[40] Z. Chen, L. Christensen, J.R. Dahn, Journal of the Electrochemical Society 150 (8) (2003).
[41] A. Jaworek, Journal of Materials Science 42 (1) (2007) 266–297.
[42] A. Jaworek, A. Krupa, M. Lackowski, A.T. Sobczyk, T. Czech, S. Ramakrishna, S. Sundarrajan, D. Pliszka, Journal of Electrostatics 67 (2–3) (2009) 435–438.
[43] L. Wang, H.W. Xu, P.C. Chen, D.W. Zhang, C.X. Ding, C.H. Chen, Journal of Power Sources 193 (2) (2009) 846–850.
[44] Y. Yu, J.L. Shui, Y. Jin, C.H. Chen, Electrochimica Acta 51 (16) (2006) 3292–3296.
[45] Y. Yu, L. Gu, A. Dhanabalan, C.H. Chen, C. Wang, Electrochimica Acta 54 (28) (2009) 7227–7230.
[46] Y. Yu, C.H. Chen, J.L. Shui, S. Xie, Angewandte Chemie – International Edition 44 (43) (2005) 7085–7089.
[47] C. Chen, E.M. Kelder, P.J.J.M. Van Der Put, J. Schoonman, Journal of Materials Chemistry 6 (5) (1996) 765–771.
[48] C.H. Chen, A.A.J. Buysman, E.M. Kelder, J. Schoonman, Solid State Ionics 80 (1–2) (1995) 1–4.
[49] C.H. Chen, E.M. Kelder, M.J.G. Jak, J. Schoonman, Solid State Ionics 86–88 (Part 2) (1996) 1301–1306.
[50] M. Mohamedi, D. Takahashi, T. Itoh, M. Umeda, I. Uchida, Journal of the Electrochemical Society 149 (1) (2002) A19–A25.
[51] K. Yamada, N. Sato, T. Fujino, C.G. Lee, I. Uchida, J.R. Selman, Journal of Solid State Electrochemistry 3 (3) (1999) 148–153.
[52] A.A. van Zomeren, E.M. Kelder, J.C.M. Marijnissen, J. Schoonman, Journal of Aerosol Science 25 (6) (1994) 1229–1235.
[53] D. Bansal, B. Meyer, M. Salomon, Journal of Power Sources 178 (2) (2008) 848–851.
[54] C. Yang, Z. Jia, Z. Guan, L. Wang, Journal of Power Sources 189 (1) (2009) 716–720.
[55] S.W. Lee, S.W. Choi, S.M. Jo, B.D. Chin, D.Y. Kim, K.Y. Lee, Journal of Power Sources 163 (1 (spec. iss.)) (2006) 41–46.
[56] T.H. Cho, M. Tanaka, H. Onishi, Y. Kondo, T. Nakamura, H. Yamazaki, S. Tanase, T. Sakai, Journal of Power Sources 181 (1) (2008) 155–160.
[57] L. Wang, Y. Yu, P.C. Chen, C.H. Chen, Scripta Materialia 58 (5) (2008) 405–408.
[58] L. Wang, Y. Yu, P.C. Chen, D.W. Zhang, C.H. Chen, Journal of Power Sources 183 (2) (2008) 717–723.
[59] E. García-Tamayo, M. Valvo, U. Lafont, C. Locati, D. Munao, E.M. Kelder, Journal of Power Sources 196 (15) (2011) 6425–6432.
[60] C.S. Yang, Q. Liu, S.M. Kauzlarich, B. Philips, Chemistry of Materials 12 (4) (2000) 983–988.
[61] J. Zhang, L.B. Chen, C.C. Li, T.H. Wang, Applied Physics Letters 93 (26) (2008).
[62] C. Chen, E.M. Kelder, J. Schoonman, Journal of the Electrochemical Society 144 (11) (1997).
[63] Z.W. Zhao, K. Konstantinov, L. Yuan, H.K. Liu, S.X. Dou, Journal of Nanoscience and Nanotechnology 4 (7) (2004) 861–866.
[64] A. Timmons, J.R. Dahn, Journal of the Electrochemical Society 154 (5) (2007) A444–A448.
[65] J. Maier, Journal of Power Sources 174 (2) (2007) 569–574.
[66] I.A. Courtney, J.R. Dahn, Journal of the Electrochemical Society 144 (6) (1997) 2045–2052.
[67] J. Maier, Faraday Discussions 134 (2007) 51–66.
[68] J.S. Do, C.H. Weng, Journal of Power Sources 159 (1 (spec. iss.)) (2006) 323–327.
[69] P. Tomczyk, H. Sato, K. Yamada, T. Nishina, I. Uchida, Journal of Electroanalytical Chemistry 391 (1–2) (1995) 133–139.
[70] P. Tomczyk, M. Mosialek, J. Oblkowski, Electrochimica Acta 47 (6) (2001) 945–954.
[71] F. Li, Q.Q. Zou, Y.Y. Xia, Journal of Power Sources 177 (2) (2008) 546–552.
[72] D. Larcher, C. Masquelier, D. Bonnin, Y. Chabre, V. Masson, J.B. Leriche, J.M. Tarascon, Journal of the Electrochemical Society 150 (1) (2003).
[73] F. Jiao, J. Bao, P.G. Bruce, Electrochemical and Solid-State Letters 10 (12) (2007).
[74] M. Gaberscek, Journal of Power Sources 189 (1) (2009) 22–27.